UNIVERSITY OF CALIFORNIA

Santa Barbara

Towards Plasmonic Solar to Fuel Conversion

A Thesis submitted in partial satisfaction of the

requirements for the degree Master of Science

in Chemistry

by

Dayton Thomas Horvath

Committee in charge:

Professor Martin Moskovits, Chair

Professor Galen D. Stucky

Professor Peter C. Ford

Professor Horia Metiu

Professor Trevor Hayton

June 2015

The thesis of Dayton Thomas Horvath is approved.

_____

Galen D. Stucky

_____

Peter C. Ford

_____

Horia Metiu

_____

Trevor Hayton

_____

Martin Moskovits, Committee Chair

June 2015

Towards Plasmonic Solar to Fuel Conversion

ACKNOWLEDGEMENTS

I would like to express my gratitude to Dr. Martin Moskovits, who showed me how much there is to learn in chemistry and in life. His positive attitude and wonderfully rich anecdotes have painted a more humorous and interesting view of the world over the past few years. I'd also like to thank Dr. Galen D. Stucky, who took me in as a wide-eyed student fresh out of undergraduate, and guided me at crucial moments to study what inspired me. I'd also like to thank the members of my doctoral committee: Dr. Peter Ford, Dr. Horia Metiu, and Dr. Trevor Hayton, for putting up with my uncertainty and giving valuable advice when it was needed most.

This work would not have been possible without the extensive help and support of the past and present members of the Moskovits and Stucky research groups. In particular, Sylvia Joun Lee and Syed Mubeen were instrumental in getting me acquainted with the techniques and methods necessary to carry out this work. The work of tireless undergrads over the last two years really made this project into a collaborative effort that made research more enjoyable and productive, thanks go to Kathleen Pacpaco, Carina Hahn, Jason Lipton, Jeffrey Lu, and Kevin Young. From the Moskovits group: Jose Navarrete, Katherine Kanipe, Brian Evanko, Will Elliott, Chris Siefe, Chrysafis Andreou, and Nirala Singh. From the Stucky group: Woo-ram Lee, Tracy Chuong, Damien Kudela, Chi Nguyen, Binghui Wu, Young-Si Jun, and Katherine Mackie. All these people have taught me so much and left me with fond memories of our time in the lab. I'd also like to thank Guang Wu, Mark Cornish, Stephan Kraemer, Aidan Hopkins, Brian Thibeault, Tony Bosch, Cabe Fletcher, Amanda Strom, and the entire Chemistry Machine Shop for being the physical and logistical support network that makes research like this a reality.

My friends and family have been eternally supportive and understanding of this journey through graduate school. In particular, Jeff Heckey and Jonathan Nelson for the many barbecues and adventures. To my father, who once upon a time taught me the plumbing and mechanical skills that I found were necessary in keeping things operational in the lab. My mother for her endless care packages, filled with love in the form of chocolate and Hungarian delicacies.

This study was made possible by the National Science Foundation, the Materials Research Lab at UCSB, and the Department of Chemistry and Biochemistry.

ABSTRACT

Towards Plasmonic Solar to Fuel Conversion

by

Dayton Thomas Horvath

The need to renewably store and utilize energy from chemical bonds has grown with recent economic and environmental concerns. Plasmonically-enabled devices have shown promise in various photosynthetic processes due to their scalable, cost-effective, and robust performance. Utilizing charge carriers derived from localized surface plasmons, these devices can drive various photoelectrochemical (PEC) reactions, however at limited efficiencies due to incomplete solar absorption. To improve broadband solar absorption in wide bandgap semiconductors, the plasmon resonance of different metal nanostructures in the visible are synthesized using anodic and sol-gel templating methods. Preliminary results suggest that gold nanoparticles and helical metal nanowires are well suited for photosensitization of titania for visible light absorption. Characterization by UV-Visible spectrophotometry, scanning electron microscopy, and photoelectrochemical measurements indicate that these templated methods can be utilized as the basis for synthesizing a variety of photoelectrochemical devices as well as unique plasmonic materials for applications including energy storage, sensing, and catalysis.

Table of Contents

Chapter 1: Introduction

1.1 The State of Energy Consumption and Production

The state of California consumed 2239 Terawatt-hours (TWh) of energy in 2012. To compare, the entire United States consumed about 27,832 TWh, or about 12.5 California's worth of energy, while the entire world consumed about 152,476 TWh, or 68 California equivalents in the same year. Figure 2 shows the general trends for worldwide energy consumption in the next twenty-five years, with worldwide consumption increasing dramatically in comparison to consistent US usage.

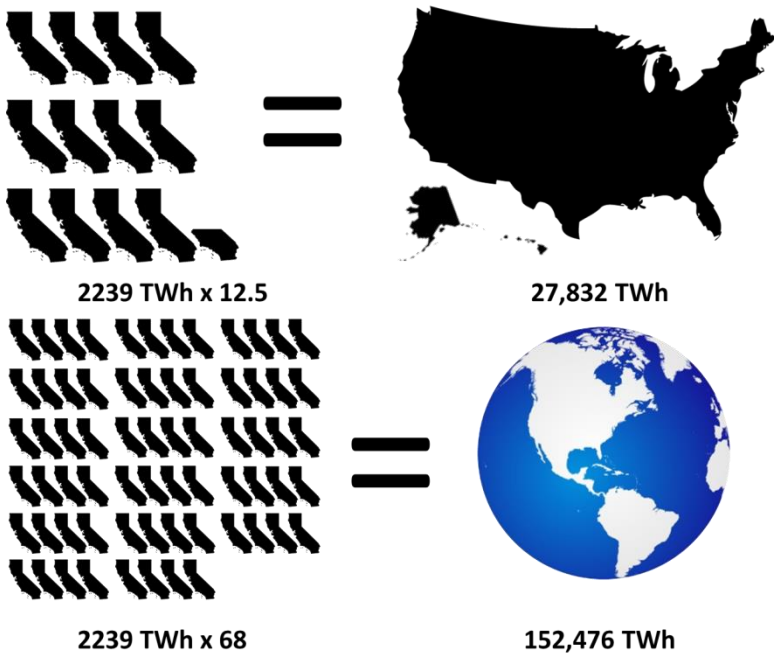

Figure 1: 2012 energy consumption as reported by the U.S. Energy Information Administration

This trend is generally attributed to the growth and development of less industrialized nations that will attain higher living standards, resulting in higher projected energy consumption. This higher standard of living is often quantified as gross domestic product per person, and is directly proportional to the per person release of carbon dioxide. By comparing these two

metrics according to each nation in Figure 3, it shows that emissions per person are proportional to income per person. More importantly, certain populous countries such as India, China, and Indonesia are distant in terms of income and CO_2 emissions, suggesting that they will be among the largest contributors to the projected energy consumption in Figure 2.

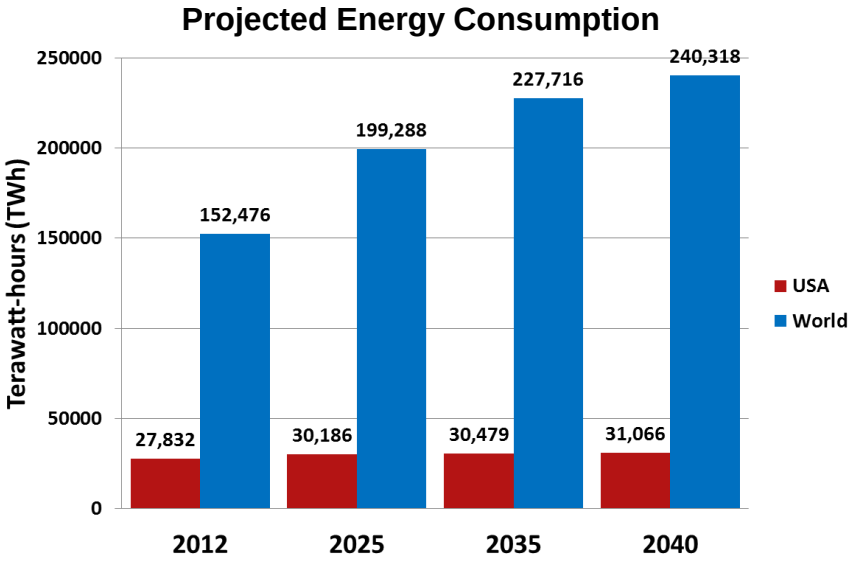

Figure 2: Projected energy consumption as reported by the U.S. Energy Information Administration

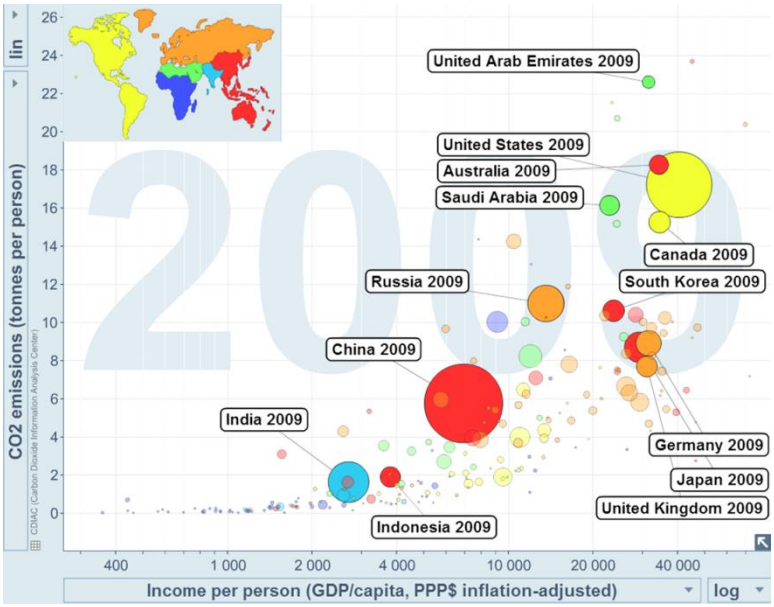

Figure 3: Increasing CO_2 emissions with income. Diameter = Yearly CO_2 emissions for that nation. Graph adapted from gapminder.org

The impending increase in CO_2 emissions towards an unprecedented 400ppm level has increased concerns towards climate change and the current distribution of (primarily non-renewable) energy sources.

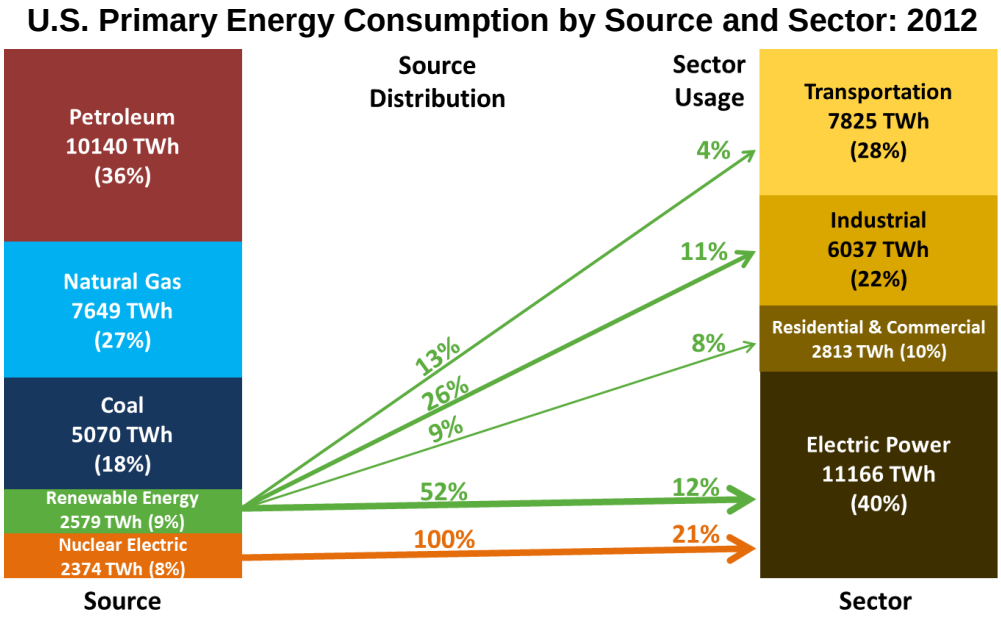

Figure 4: 2012 Distribution of energy sources and uses in the U.S. Graph adapted from the Jan. 2014 Monthly Energy Review published by the U.S. Energy Information Administration

All the nuclear power in the U.S. only makes up 21% of the electric power sector, illustrating the minimal use of this technology in recent decades. The Fukushima Daiichi nuclear disaster has been cited as a recent reminder as to why nuclear power is not a viable alternative to standard hydrocarbon energy sources. When compared to the estimated health impacts of coal and natural gas however, nuclear ranks lower in terms of years of human life lost even accounting for the Fukushima disaster. Figure 5 compares the disaster (4,800 years of human life) in addition to the years of human life lost in producing one Fukushima complex-lifetime's worth of energy (22,000 years of human life) with a much more disturbing amount for coal generation for that same energy amount. Even using natural gas has a higher societal cost compared to nuclear including the 2011 disaster.[1]

Estimated Years of Human Life Lost		
Fuel Type	1 TWh	898 TWh
Coal	138	124,000
Gas	42	38,000
Nuclear	25	22,000
Nuclear + Fukushima	30	26,800

Figure 5: 2012 The estimated cost of human years of life lost per Terawatt-hour of energy produced using each primary energy source. The values in the third column are scaled to the Fukushima reactor complex capacity over the life of the reactor.[1]

Despite this, governmental regulations have turned the energy sector's focus to renewables. Of all the primary energy sources in Figure 4, only 9% come from renewable sources such as biomass (4.2%) and solar (5.1%). Biomass as a whole is inefficient from solar to fuel and land use perspectives, while solar has no complementary technology to store energy at grid scale. In regions such as California that lead the renewable energy segment with solar panel implementation, this lack of storage has resulted in an emerging consistency problem. Peak demand for electricity occurs in the evening as shown in Figure 5, just after peak production from solar panels drastically decreases, putting increased demand on non-renewable sources. As more solar panels are implemented, this daily increase in demand will get steeper, ultimately limiting the use of solar as a reliable and renewable power source. Although the state of California has put out mandates to construct grid-scale storage, no single energy storage technology exists at this scale that can release energy as quickly as natural gas.

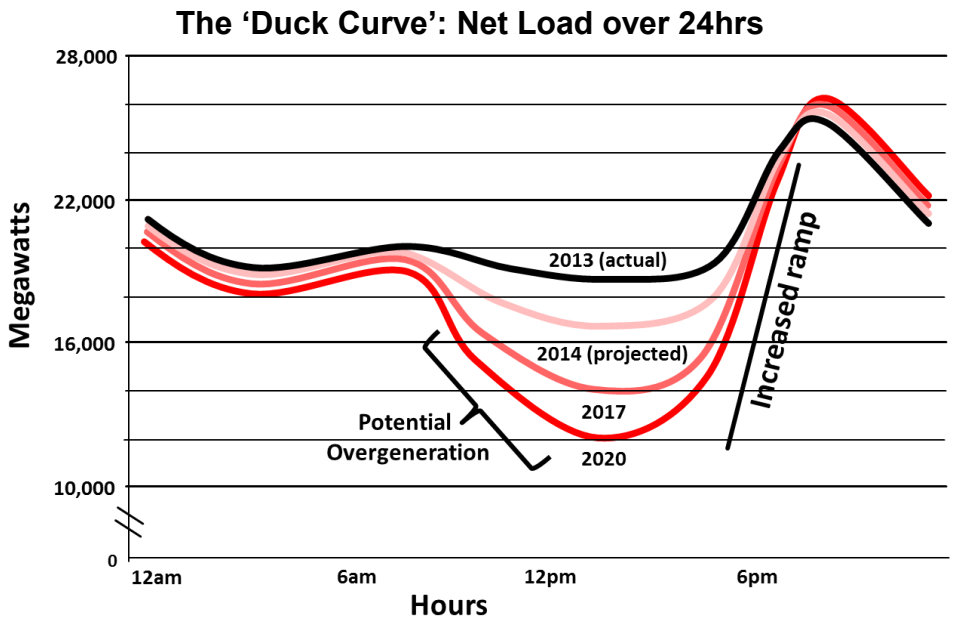

Figure 5: Net load over 24 hours in California as reported by the California Independent System Operator

This leaves the renewable energy component of U.S. energy production at a severe disadvantage to the readily storable and efficient hydrocarbon energy sources. Furthermore, the various disadvantages of each energy source may explain the diversified nature of US energy production at present. To make energy sources renewable and storable would require recycling carbon dioxide or other waste components into fuels such as methanol and methane. Driving these reactions requires the only abundant source of renewable energy: solar. Photocatalyzed reduction of carbon dioxide to simple fuels or splitting of water to hydrogen can increase the renewable and storable part of energy production in Figure 6 while reducing coal use. This concept is reflected in recent publication trends in peer-reviewed journals and patent applications. Figure 7 shows a drastic increase in the number of published works in recent years, with US research contributions a distant third to Chinese and Japanese research in this area.[2]

The need for improved solar to fuel technologies is evident from environmental, economic, social, engineering, and scientific perspectives. Deciding which fuel to produce

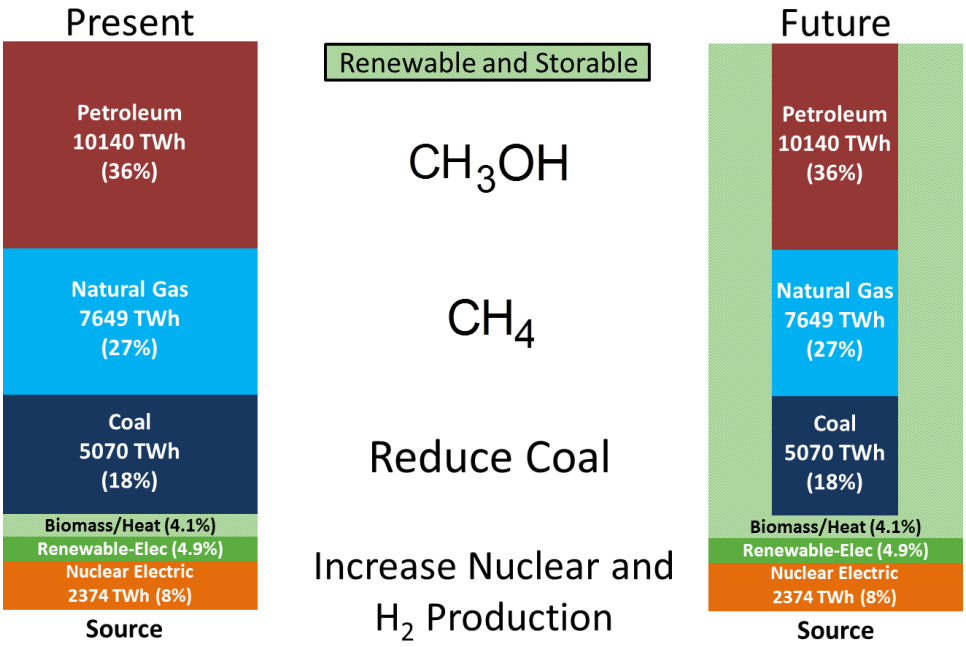

Figure 6: 2012 energy sources and future renewable potential in the U.S. Graph adapted from the Jan. 2014 Monthly Energy Review published by the U.S. Energy Information Administration

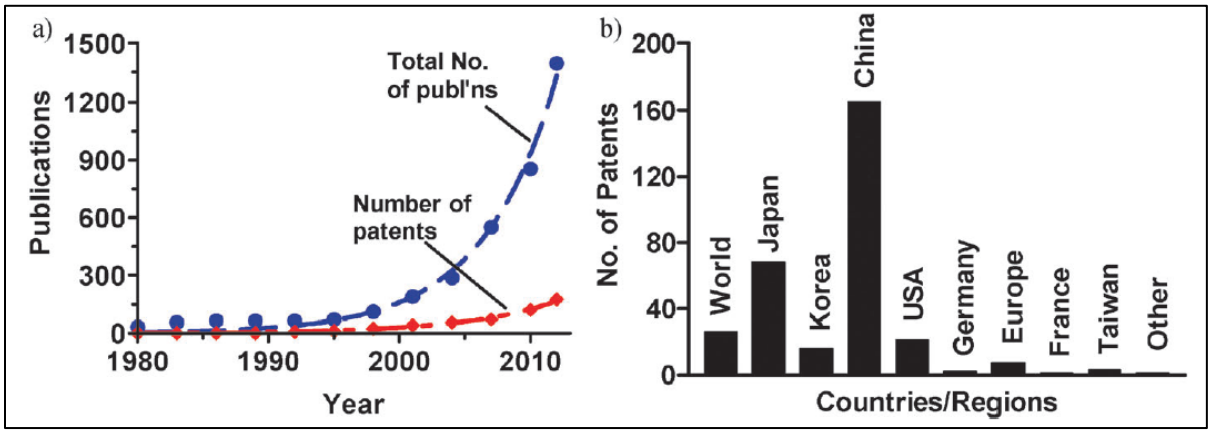

Figure 7: Publications and patents on the photocatalyzed production of hydrogen from water and fuels from carbon dioxide.[2]

has been debated for years, and although there may not be complete agreement in the reaction of choice, there are limited sensible options when considering the scale at which these simple fuels are currently produced.

1.2 Solar to Fuel Technologies

Methanol is one of the most greenhouse gas intensive production processes after

Figure 7: Greenhouse gas emissions and production volumes for top 18 large volume chemicals. Based on IEA graph from Technology Roadmap: Energy and GHG Reductions in the Chemical Industry via Catalytic Processes© IEA 2013, IEA Publishing; modified by Dayton T. Horvath. License: http://www.iea.org/t&c/termsandconditions/

ammonia and ethylene. Considering production volume and molecular composition relative to carbon dioxide, the single carbon alcohol is a good target fuel that also aligns well with current transportation and consumption infrastructure. A quick overview of solar to fuel reactions compared to water splitting shows the relative difficulty in electrochemically producing more reduced products such as formic acid, methanal, methanol, and methane in

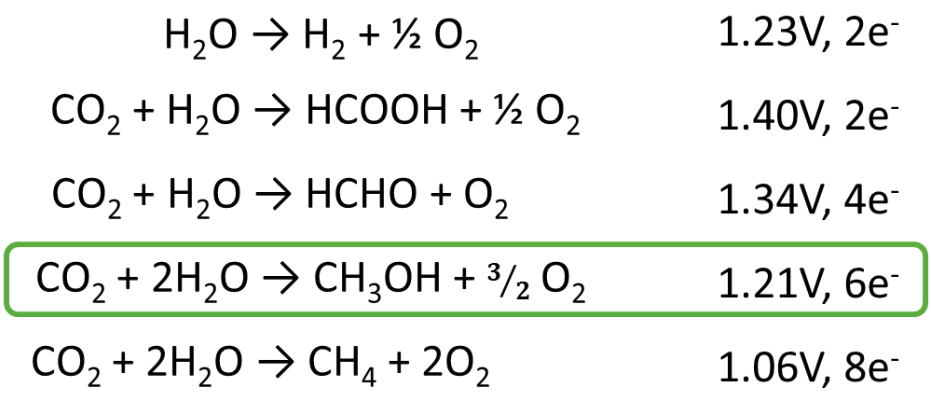

Figure 8: A comparison of reduction reactions and their overpotential/electron count requriements.[3]

an aqueous environment. Water splitting has been studied extensively as a test reaction due to its experimental simplicity, but ultimately isn't ideal because of the energy expended on producing oxygen in addition to hydrogen. In the case of carbon dioxide reduction, electrons and protons are required from an oxidation half reaction, which in some cases is hydrogen gas. The gas-phase nature of carbon dioxide at room temperature and pressure along with limited solubility in water makes conversion particularly difficult to carry out and monitor experimentally. The possibility of intermediates and multiple products increases with the number of electrons required in the reduction, adding to experimental complexity and scalability concerns. Lastly, catalytic over-potentials and low turnover rates might explain why methanol is commercially produced at high temperatures at significant energy cost but with high turnover and conversion efficiency. Photoelectrolysis of carbon dioxide to methanol is still fully in the research stage of development but is not inherently limited by long-term stability and high energy requirements. By investigating photoelectrolysis in atmospheric conditions, the ultimate application in a solar-type installation can be tested without the need for advanced in-situ experiments.

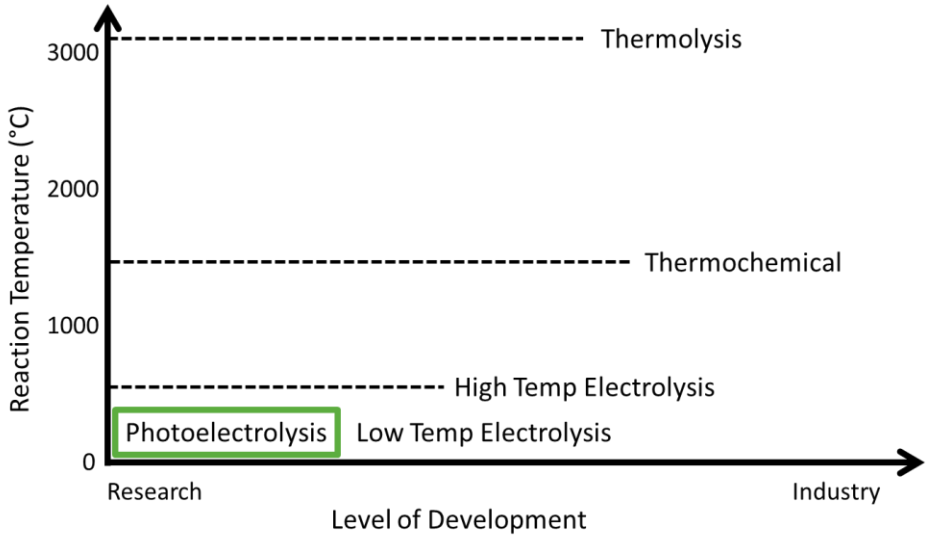

Figure 9: Carbon dioxide to methanol conversion technologies

There are four primary requirements for a solar to fuel device to be effective. The light absorber, usually a semiconductor, must have a bandgap between 1.6eV and 2.2eV to accommodate over-potentials and absorb visible light. Catalyst over-potentials are inherent inefficiencies in the materials used to drive a reaction, and just under half of the solar spectrum's irradiance is in the visible. Second, the valence and conduction bands of the semiconductor must align with the redox potentials for the reaction in question. Efficient charge generation, transfer, and reaction kinetics ensure that the energy is converted into reaction products. Lastly, the device must be stable in aqueous solution to ensure conversion over years of use.[4] The research goals for this technology are also four-fold: to make a scalable, inexpensive, stable, and efficient device. Each of the schemes represented in Figure

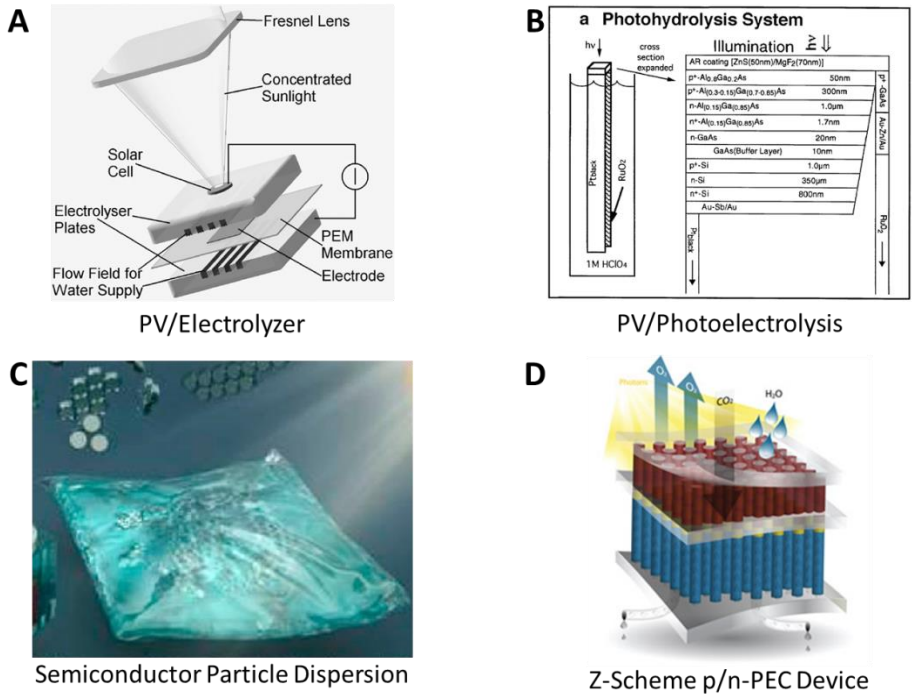

Figure 10: Solar to fuel device schemes A: Photovoltaic coupled to an electrolyzer[5] B: Photovoltaic combined with electrocatalysts in solution.[6] C: Semiconductor nanoparticle dispersion[7] D: Z-scheme p-type/n-type tandem photoelectrochemical device as envisioned by the Joint Center for Artificial Photosynthesis (JCAP)[8]

10 achieve two of the device goals. For example, a standard photovoltaic electrically connected to an electrolyzer using precious metal catalysts achieves 18% overall solar to hydrogen efficiency with good lifetime, but scalability and fabrication costs are prohibitively expensive.[5] A step in the right direction is shown in Figure 10 B where the electrocatalysts are deposited directly onto the photovoltaic, generating over 18% solar to hydrogen efficiency in a self-contained system but with the same drawbacks as the scheme in A.[6] Semiconductor particle dispersions are an attractive model because they are scalable and inexpensive but have limited efficiency and lifetime.[7] A promising compromise between other methods is depicted in Figure 10 D as a z-scheme (two semiconductor) device with matched bandgaps to absorb the largest portions of the visible spectrum and drive oxidation and reduction half reactions on separate sides of a semipermeable membrane.[8] The main

concern with this design is using materials that are robust, yet abundant and can give a competitive efficiency on the order of 1%-5% solar to hydrogen.

All these devices are benchmarked using water splitting because electrocatalysts in that field have been well studied, the reactant is the solvent, and the produced hydrogen is a necessary step towards more difficult carbon dioxide reactions. The ultimate issue with semiconductor light absorbers in any of the above devices is that the best absorbers are not scalably grown and photocorrode[9], while the robust absorbers have the wrong bandgap for visible absorption and poor charge transport properties. At present, materials such as silicon and gallium arsenide have been shown to retain efficiency over multiple days only with protective oxide coatings that reduce performance.[10]

1.3 Plasmonics for Solar to Fuel Applications

Conductive materials can exhibit two general types of surface plasmons depending on geometry and size.[11] Surface plasmon polaritons occur at a planar metal-dielectric interface, while localized surface plasmons occur in nanostructured materials. These localized surface plasmons resonate at the frequency of absorbed light, generating intense electric fields on the surface of nanoparticles or other nanostructures as shown in Figure 11. These electric fields have found numerous applications for surface enhanced Raman spectroscopy (SERS) amongst other sensing techniques.[12]

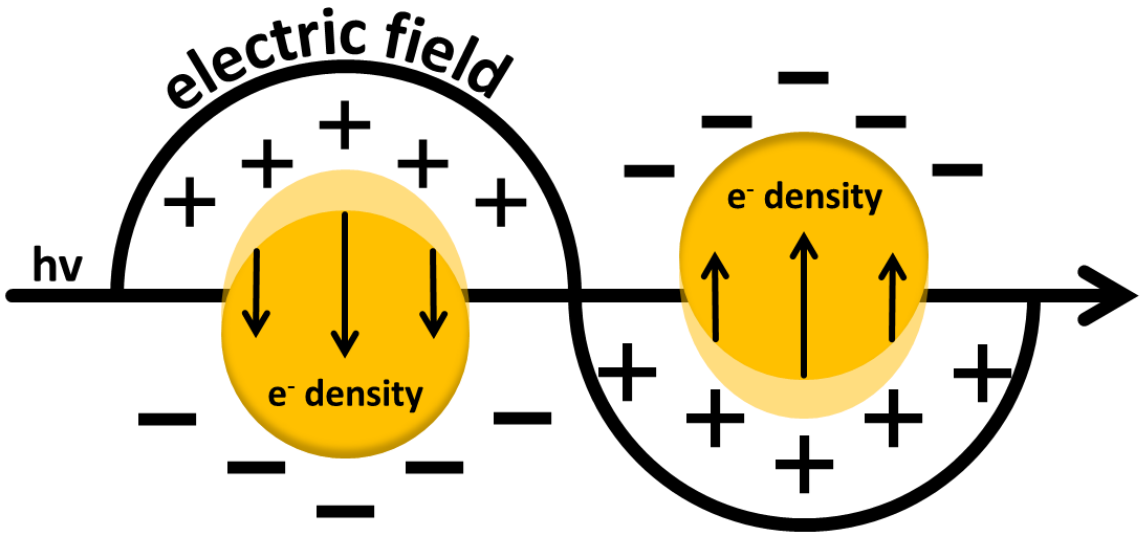

Figure 11: Localized surface plasmon resonance showing oscillations of electrons due to electromagnetic waves

When these electric fields decay on the order of 1-100 femtoseconds, the energy dissipates through radiative emission, or through the more preferred path of hot electron generation. These energetic electrons are termed 'hot' because they exist at the top of a Fermi distribution of electron energies in conductive nanostructures. Most often observed in gold or silver nanoparticles and nanorods, these hot electrons may be injected into the conduction band of an appropriate semiconductor such as titania. An ideal semiconductor has an electron affinity below the Fermi level of the metal, forming a Schottky barrier that the hot electrons overcome. A small percentage of these hot electrons succeed in becoming charge carriers in the semiconductor conduction band as shown by the red arrow in Figure 12. This occurs at a reduced energy requirement compared to the standard bandgap of the semiconductor and absorbing light of lower energy than would otherwise be possible. An alternate, though much less likely, non-radiative path for the same hot electrons is to tunnel through the Schottky barrier into the semiconductor as seen by the dotted arrow in Figure 12.[13]

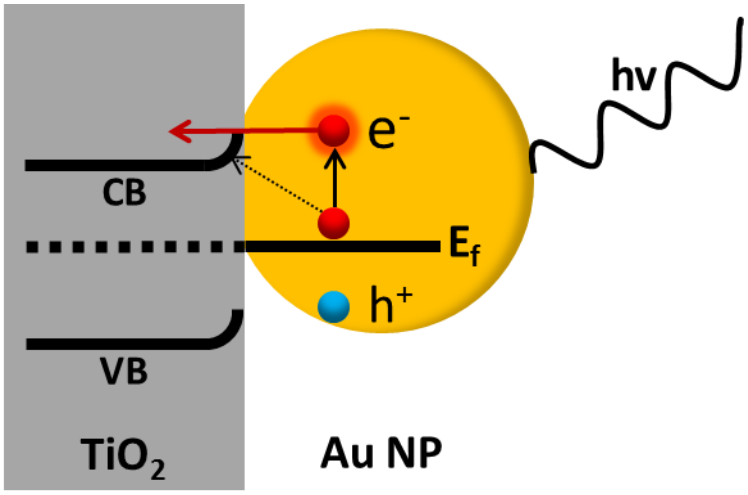

Figure 12: Wide bandgap semiconductor (TiO_2) photosensitization by plasmonic nanoparticle (Au) through hot electron injection (solid arrow) or tunneling (dotted arrow).

To continue this process, a constant source of electrons must be provided in order to prevent positive charge buildup in the metal nanostructure. Recent research has taken advantage of this metal/semiconductor Schottky barrier as a method of photosensitizing wide bandgap semiconductors with plasmonic nanostructures in an effort to capture a larger portion of the solar spectrum.[14]

Plasmonic nanostructures are beneficial as light absorbers because of their broad spectrum absorption that can be tuned with various geometries and compositions. Other benefits include a high absorption coefficient and a different set of governing principles in determining theoretical efficiency. Plasmonic photovoltaic or photocatalytic devices can be fabricated to match the solar spectrum using minimal amounts of material without concern for limiting efficiency as compared to highly variable absorption coefficients across the spectrum in silicon-based photovoltaics. This matching can be done by choosing the right metal (gold, silver, palladium, aluminum) and varying the dimensions of the nanorods or nanoparticles.[15] Synthetic control over nanostructure size is a crucial requirement in selecting the right method for templating and growth.

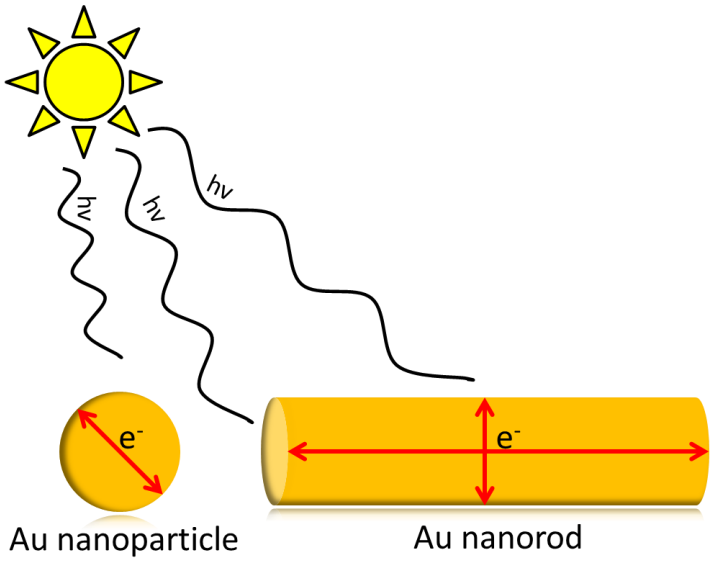

Figure 13: Localized surface plasmons are generated in nanoparticles and in nanorod transverse and longitudinal axes when illuminated.

The theoretical efficiency of plasmonic photosensitization further qualifies this method of light absorption as a viable alternative to semiconductors for solar to fuel applications. Given a number of assumptions outlined elsewhere[16], light absorption in metallic nanostructures interfaced with a semiconductor could give upwards of 10% energy conversion efficiency. Although other reports suggest higher theoretical hot-electron efficiencies, even up to 22%[13], the other three device goals must be taken in context. Plasmonic metals and wide-bandgap semiconductors can be selected to be functionally stable for over 60 hours with no measurable decrease in operation[17], and device fabrication is scalable at cost due to the minimal amounts of noble metals required. The crucial stability that semiconductors have lacked thus far is a given trait with plasmonic hot electron generation. It has been posited that an efficiency as low as 1% might be commercially viable given the longevity possible with plasmonic solar to fuel production.[18] To be just in comparing this to semiconductor light absorption, the different solar to fuel schemes presented in Figure 10 have theoretical efficiencies limited primarily by the photovoltaic

component of the system. The theoretical efficiency of single junction silicon photovoltaics is about 29% with experimental efficiencies exceeding 25%. The z-scheme tandem devices have a theoretical efficiency of 21.6%.[19] The difference between experimentally proven efficiencies and theoretical efficiencies are orders of magnitude larger for plasmonic devices compared to semiconductor-based charge carrier generation, indicating that plasmonic solar to fuel research is still in its infancy.

Valve metals such as titanium, aluminum, tungsten, and tantalum all exhibit self-terminating oxide surface films that provide great corrosion resistance for the underlying metal. This oxide film is a key requirement in the anodization of these metals into nanostructured porous metal oxide films. Anodization of titanium to form these structures can be carried out in a two electrode arrangement in fluoride containing polar organic solvents. Titanium acts as the anode, undergoing room temperature oxidation and preferential etching to form nanotubular structures when a potential is applied. The last decade has shown hundreds of reports detailing synthesis and application of titania nanotube arrays (TNA) for gas sensing, drug elution, dye-sensitized solar cells, photoelectrochemical water splitting, and photocatalytic reduction of carbon dioxide.[20] Films with varying crystallinity, pore diameter, aspect ratio, base substrate, and morphology make it a highly customizable templating platform. Anodization of titanium alloys results in doped titania nanotube arrays that exhibit better absorption, catalytic, or sensing properties due in part to the thickness of the nanotube walls being on the order of 20nm, less than the diffusion length of minority carriers in anatase titania. By losing fewer holes to recombination over $30 m^2/g$ surface area in aqueous or gas phase applications, more efficient charge transfer takes place than compared to nanoparticles.

Water splitting using these nanomaterials was reported in a tandem architecture consisting of n-type TNA as the photoanode and p-type copper-doped TNA as the photocathode. The instability of the copper doped component of the system and low solar to hydrogen efficiencies below 0.5% are major drawbacks of the system.[21] Instead of doping the TNA with various elements to shift the wide 3.2eV bandgap of anatase titania into the visible, photosensitizing TNA with plasmonic nanostructures nearly eliminates photocorrosion and absorbs a wider portion of the visible spectrum. Plasmonic enhancement of photocatalytic water splitting using visible light has been demonstrated using electron beam deposition to decorate TNA with gold nanoparticles.[22] Nanostructured gold exhibits a localized surface plasmon resonance in the red portion of the visible spectrum, a particularly difficult region to achieve maximum absorption using semiconductors. Another reported method of Au nanoparticle decoration begins with a titanium-gold alloy that was anodized to form TNA with 5nm gold nanoparticles interspersed in the semiconductor. The hydrogen production efficiency of these devices was similarly low, demonstrating another method for photosensitizing titania with gold.[23] Chemical reduction of metal-containing solutions has also been used to deposit noble metal nanoparticles into TNA for enhanced photocatalytic dye degradation[24] as well as for SERS substrates.[25] These efforts and more all aim to take advantage of the visible absorption provided by gold nanostructures. However, the extent of loading and the quality of the titania-gold interface are not easily quantified in these scenarios.

One of the most common methods for templating metal nanostructures in device form is anodization of high purity aluminum. Anodic aluminum oxide (AAO) is formed through electrochemical oxidation of the surface to produce vertically aligned, hexagonally arranged

pores with controlled diameter and aspect ratios. The process involves a two electrode system with applied voltage between the aluminum working electrode and a counter electrode in acidic aqueous solution.[26] These films have been used widely for the synthesis of ordered nanostructures with excellent control over template dimensions. Various types of electrodeposition can be used to fill these pores with metals or semiconductors in a low-cost and scalable fashion. The resulting arrays can be liberated from the template using phosphoric acid or sodium hydroxide to dissolve the AAO. One challenge in successfully electrodepositing certain materials into AAO is the barrier layer found at the bottom of the pores. Without ohmic contact between the solution and the underlying aluminum, standard plating methods must be preceded by thinning or complete removal of the aluminum oxide barrier layer. Both chemical and electrochemical methods have been reported to remove this 20nm to 80nm thick layer.[26] This technique has been shown to be most effective when working with thin films of aluminum electron-beam deposited onto transparent[27] and/or conductive substrates.[28] Precise control of pore diameter, aspect ratio, and barrier layer thickness enable fabrication of gold nanorod arrays as the basis for a photoelectrochemical device.[29] Utilizing oxygen evolution and hydrogen evolution catalysts such as cobalt oxide and platinum, an autonomous device for plasmonically driven water splitting has been reported from this fabrication scheme.[17]

One of the more exotic uses of AAO templating for nanostructure formation was demonstrated using a block copolymer-directed sol-gel technique. The confinement of the block copolymer silica sol-gel solution inside anodic aluminum oxide pores generated unique helical and stacked doughnut-like mesoporous silica.[30] Subsequent AC-electrodeposition of silver revealed the range of unique nanostructures that formed as a function of pore diameter.

The resulting silver nanostructures are effective as substrates for surface-enhanced Raman spectroscopy (SERS) but little characterization of their optical properties was reported.[31]

Chapter 2: Experimental

2.1 Synthesis of Titania Nanotube Array Photoanodes:

Titanium Substrate:

Titanium foil (99.7%) was purchased from Alfa Aesar at 0.89mm thickness. Coins were machined approximately 30mm in diameter and manually polished using silicon carbide sandpaper (600, 1200, 1500, 2500 grit). First anodization was performed in a preconditioned ethylene glycol or glycerol solution containing 0.5wt% ammonium fluoride and 0.2wt% deionized water. Preconditioning of the solution by running a 24-hour anodization of a titanium sample increases conductivity via dissolution of titanium into the solution, accelerating anodization when the solution is reused. Anodization at 50V using a DC power supply and a graphite counter electrode was carried out for at least four hours. The TNA film that formed was peeled off with tape or was etched away in 1:1 v/v deionized water/37% hydrochloric acid while sonicating for 15 minutes. The second anodization was performed under identical conditions for about three hours.

Fluorine-doped Tin Oxide (FTO) Substrate:

FTO on glass was purchased from Sigma Aldrich (13Ω/sq, 2.3mm thick) and sectioned for ease of titanium deposition. A Temescal CV-6S electron-beam evaporation system was used to deposit 500nm at 0.5nm/sec onto FTO pieces approximately 20mmx25mm in area. Only one anodization was performed on these samples due to the minimal amount of titanium present. Pore widening of the TNA pores using 2.0M hydrochloric acid was carried out prior to electrodeposition to form similar diameter pores to the two-step anodization pores.

Gold electrodeposition on TNA:

Pulsed electrodeposition was carried out using an EG&G Princeton Applied Research (Model 273A) potentiostat running custom labview software for pulsed galvano/ potentiostatic three electrode cells. A commercial neutral-pH OROTEMP 24 gold electroplating solution from Technic, Inc. was used for gold nanoparticle deposition onto TNA samples. Galvanostatic pulsed deposition was held for one second at 20 mA/cm^2 followed by a seven second delay, repeating the cycle 20-40 times.[32]

All samples were annealed in flowing air at 450°C prior to testing in a three-electrode electrochemical cell.

2.2 Synthesis of Mesoporous Silica-templated Metal Nanostructured Arrays

Anodic aluminum oxide fabrication:

Puratronic aluminum foil (99.997%) was purchased from Alfa Aesar at 0.25mm thickness. Coins approximately 30mm in diameter were cut from the sheet according to the size of the copper back contact used in a custom-built anodization cell. An optional 500°C heat treatment in vacuum for 3 hours increases aluminum grain size for better uniformity across the sample. Electropolishing of these coins was performed in a 4:1 v/v ethanol: 70wt% perchloric acid at 5°C for 5 (may vary from 3 min-10 min) minutes while stirring. A high voltage DC power supply with ammeter and volt meter was used to apply 20V (may vary from 8V-20V if power supply is current limited) to the aluminum anode and similar area or larger graphite cathode.

A first anodization was carried out at 40V DC using the same power supply as for electropolishing. The aluminum coins were placed in a custom Teflon and lexan

polycarbonate electrochemical cell using copper stubs as back contacts. Alternately, the coins or squares could be masked with 3M electrochemical anodization tape (3" width) and back contacted with double sided copper tape (1/2" width). A good seal is vital to prevent shorting and anodization of the copper instead of the sample. All anodizations were performed using a graphite counter electrode in 0.3M oxalic acid at about 4°C while stirring. The first anodization was run for 2.5 to 8 hours under light stirring in an ice bath and/or a temperature controlled chiller.

The AAO layer formed by first anodization was removed by chromic acid etch at 50°C for 6-18 hours depending on thickness of film. The chromic acid solution was prepared with 1.5g chromium (VI) oxide and 6g of 6 wt% phosphoric acid diluted to 0.1L volume. A second anodization was performed for 12min to 15min depending on thickness desired (1μm to 1.5μm) under identical conditions to the first anodization. Following this, a pore widening etch was performed in 5wt% phosphoric acid between 45 and 60 minutes. Barrier layer thinning was carried out on some samples following a current reduction protocol.[33] The anodization voltage was reduced from ≈27V to ≈10V over a 15 minute period to maintain 290μA/cm^2 current density. A step down to 135μA/cm^2 for 15 minutes followed until voltage decreased to ≈6V.

Mesoporous silica sol-gel templating

Two solutions were prepared separately and then combined as part of the sol-gel process. Solution one contained 2.7 mL deionized water adjusted to pH 2 with concentrated hydrochloric acid, 5.06mL of ethanol, and 5.59mL of tetraethyl orthosilicate (TEOS) stirred until uniform. Solution two contained 7.6mL of ethanol with 1.38g Pluronic 123 (P123)

block copolymer stirred until clear. Solution one and two were combined and stirred for four hours in a sealed beaker. Samples were dip coated using tweezers at a rate of 12cm/min (approximately 10 seconds down and 10 seconds up) and then spun on a spincoater at 3000rpms for 10 seconds to remove excess solution. Samples were allowed to age for 24 hours prior to heat treatment in air at 500°C for one hour with a 1°C/min ramp rate.[30]

Electrodeposition methods:

AC electrodeposition of silver was carried out using an Agilent AC power source analyzer (Model 6811B) with the AC Source GUI software (Ver. A.01.08). A two electrode setup with a graphite counter and the sample as working electrode were immersed in a solution of 0.5M boric acid and 0.05M silver nitrate in 100mL water made fresh every time. The solution was stirred while 40V ($28.28V_{rms}$), frequency 1kHz, was applied for 5-30 minutes. AC electrodeposition of gold was carried out in a similar fashion using a solution of pH 1.5 adjusted 1g/L hydrogen tetrachloroaurate tetrahydrate and 30g/L (0.5M) boric acid.[30]

Pulsed electrodeposition of silver was carried out using a Biologic VSP potentiostat in a three electrode arrangement with a saturated calomel reference electrode and platinum counter electrode. The more concentrated solution contained 200g/L diammonium hydrogen citrate and 105g/L potassium thiocyanate, followed by dropwise addition of 8.5g/L silver sulfate. The pH must be about ≈4.5 prior to silver addition. While stirring, a pulse train of galvanostatic 6ms at -15mA/cm^2, potentiostatic 6ms of +6V, and 0.4 sec-1 sec delay were collectively repeated 5,000-15,000 times for 1μm -3μm thick AAO samples.[34]

A polydimethylsiloxane (PDMS) encapsulation followed by aluminum removal using galvanic replacement enabled transmittance UV-Vis spectrophotometery to be performed on

samples. The silicon elastomer was mixed in a 10:1 ratio with the curing agent into a disposable plastic cup. Mix using a metal spatula for 5 minutes at minimum. Place the cup in a vacuum container (dessicator) and cycle vacuum on and off at approximately one minute intervals until all bubbles are removed. Pour the PDMS into a clean plastic petri dish, hit petri dish on counter from at least 12 inches above the counter to dispel any remaining bubbles. Place the sample (4mm x 4mm at minimum) face down (aluminum up) on the surface of the PDMS using tweezers. Look from underneath petri dish that there are no larger bubbles directly under the samples. Heat at ≈75°C for 30-60 min. The petri dish was removed by cutting around the edges with a razor. To remove the exposed aluminum substrate, an ice bath with a beaker containing 50ml DI water and 50mL concentrated hydrochloric acid was prepared. Then 1.7g copper (II) chloride hydrate was added. The PDMS encapsulated samples were added to the beaker for 30-45 minutes and agitated occasionally to remove excess copper until the aluminum dissolved.

2.3 Characterization and Testing

All scanning electron microscopy was done using an FEI XL40 Sirion FEG Digital Scanning Microscope with EDS detector at 5kV accelerating voltage. UV-Vis spectra were taken on a Shimadzu UV3600 UV-Vis-NIR spectrometer equipped with a diffuse reflectance integrating sphere. Photoelectrochemical measurements were taken on a EG&G Princeton Applied Research (Model 273A) potentiostat running EChem DOS software. Solar radiation was replicated using a 300W xenon lamp (Newport Model 66902) powered by a Newport power supply (Model 69911) was calibrated using a silicon photodetector (Newport Model 2930C) in conjunction with AM1.5 Global and UV-420nm cutoff filters. TNA-based samples

underwent linear sweep voltammetry in 1.0M sodium hydroxide solution against a saturated calomel electrode reference and platinum wire counter electrode.

Chapter 3: Titania Nanotube Array Photoanodes

3.1 Proposed Titanium substrate-based device

A plasmonically sensitized photoanode was conceived according to available fabrication techniques and their relative capabilities. Polished titanium coin substrates were used because they offer a reusable starting point with nearly unlimited thickness for multiple anodization procedures. The device in Figure 12 is a logical starting point for investigating the plasmonic effect of gold nanoparticles for multiple reasons.

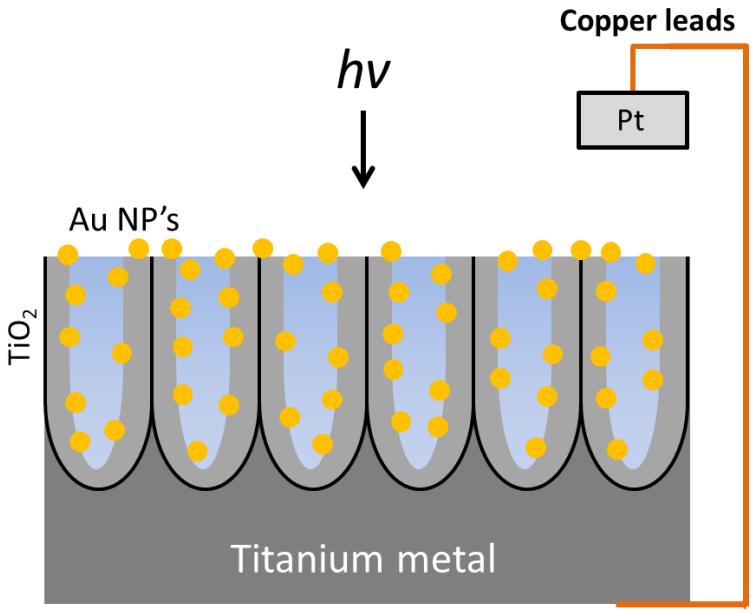

Figure 14: Proposed TNA photoanode on titanium substrate

The device requires only four major processing steps: first anodization, second anodization, electrodeposition, and heat treatment. Although relatively straightforward in processing, the anodizations proceed slowly requiring multiple days to complete in some cases. The vertically oriented nanotube arrays support charge transfer to the substrate well for having a thickness of over 4μm (considerably more than the carrier diffusion length for crystalline titania). The bench-top anodization and electrodeposition methods are readily scalable in the event large scale samples require testing. Drawbacks of this design relate primarily to the

lack of consistent TNA film growth below 4 μm in thickness, making uniform electrodeposition of gold throughout the TNA less likely. Lastly, there is minimal control over the barrier layer thickness at the bottom of the titania nanotubes. Compared to a plasmonic photoanode in the literature[29], this device has fewer, simpler, and more scalable fabrication steps and an increased titania-gold contact area when compared to atomic layer deposited films of titania on gold.

3.2 Results and Discussion

Titania nanotube arrays were produced using two step anodizations in a variety of solutions including glycerol with ammonium fluoride, ethylene glycol with hydrofluoric acid, ethylene glycol with ammonium fluoride, and even some mixed solvent combinations. The most uniform TNAs were produced using ammonium fluoride in ethylene glycol, with minimal surface debris and little variation with changes in film thickness. Small variations in the amount of water added to the polar organic solutions did not impact the morphology appreciably. Figure 15 shows a cross section of a 15 μm thick TNA film with sparsely interspersed gold nanoparticles from a pulsed electrodeposition method. Most of the gold loading was on the top surface of the TNA, with light deposition on the bottom side of the film indicating diffusion of the solution through the entire film. This suggests that wettability is not the reason for limited deposition throughout the film. Instead, the increased conductivity of the titania when a reducing bias is applied during electrodeposition created preferential nucleation where diffusion of aqueous species was least limited: the surface. Irrespective of the distribution of gold nanoparticles on the TNAs, the absorbance spectra for annealed neat TNA and TNA-AuNP samples shows a distinct peak around 700nm in Figure

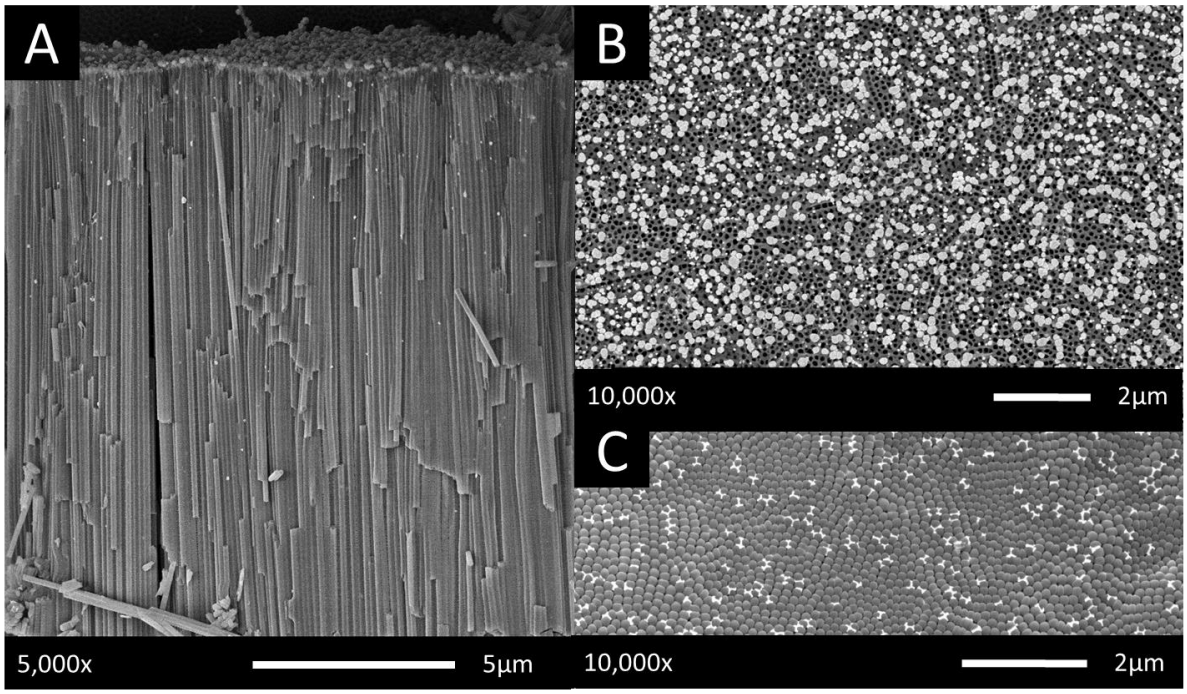

Figure 15: Electrodeposited Au nanoparticles on TNA. A: Cross-section B: Top view C: Bottom view

16. This increased absorbance in the visible is attributed to the localized surface plasmon resonance of gold nanoparticles ranging in diameter from 10nm to 80nm. Longer deposition times increase gold nanoparticle size, shifting the resonance further towards the infrared portion of the spectrum.

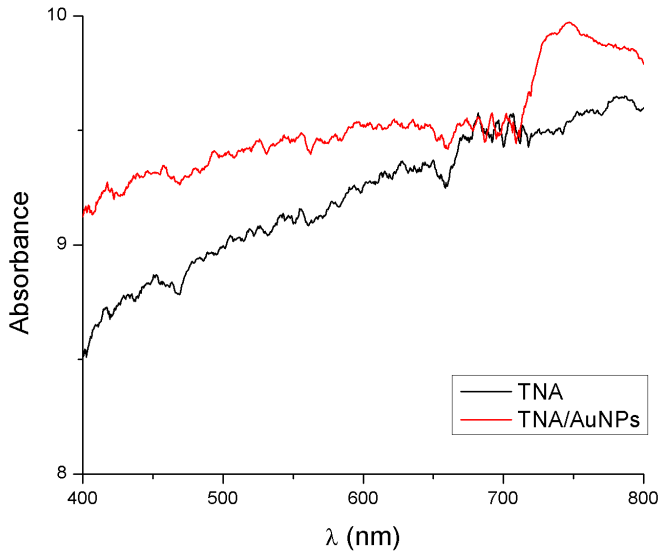

Figure 16: Visible absorbance spectra of TNA and TNA-AuNPs

Given an improved visible absorbance for the TNA-AuNP sample, an initial test for photocurrent due to visible light absorption was carried out in basic solution. The results of a linear sweep voltammogram in Figure 17 show a definite increase in photocurrent across nearly a one volt range compared to the dark current. This 20μA/cm^2 result compares respectably with published work that used a 633nm laser to excite e-beam evaporated gold nanoparticle-loaded TNA photoanodes under similar conditions.[22] The uneven and relatively low loading of the overall TNA structure with gold nanoparticles generated a measurable photocurrent, one that is expected to increase with optimization of TNA and electrodeposition parameters for maximum titania-gold contact.

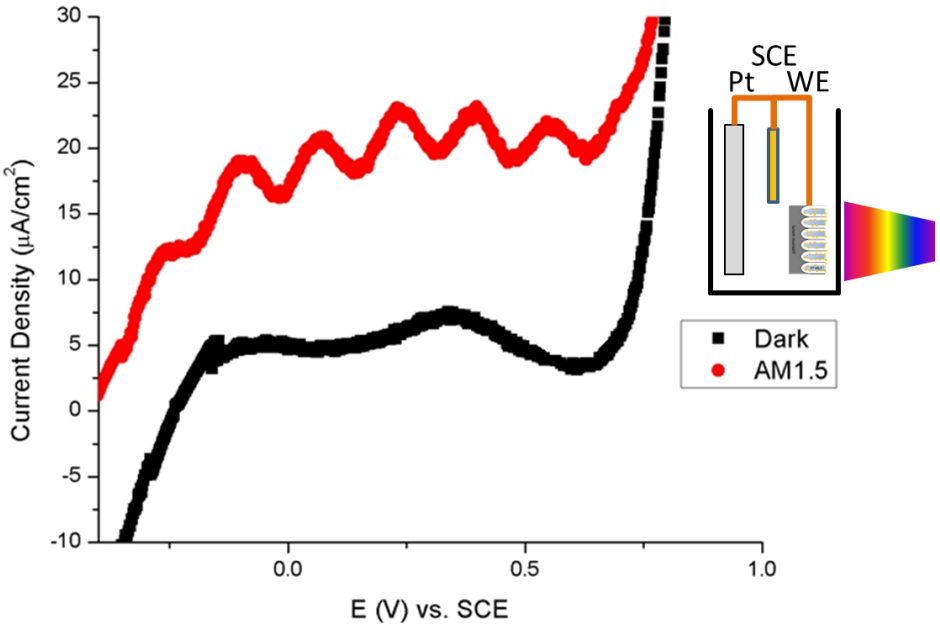

Figure 17: Linear sweep voltammogram of TNA-AuNP photoanode at 20mV/sec in 1M NaOH normalized for one sun AM1.5 solar radiation above 420nm.

3.3 Proposed FTO substrate-based device

To address the gold nanoparticle optimization issues, and open up future avenues for modification and application, a fluorine-doped tin oxide substrate was used as the foundation

for this photoanode. The transparent conducting oxide on glass is a great bottom contact for bottom-up illumination schemes if any finishing layers beyond Figure 18 are not transparent. The basic device design utilizes a single step anodization, forgoing some of the ordering and surface smoothness offered by two step anodization in favor of a much faster processing time (hours) without compromising scalability. The precise control over TNA film thickness is the result of nanometer level precision of e-beam evaporation of titanium onto the FTO substrate. Although e-beam evaporation is thickness limited to only a few microns, this shouldn't affect device function given the high absorption coefficient of gold nanoparticles. One of the only disadvantages is the lack of a titania barrier layer at the bottom of the nanotubes because of the difficulty in determining complete anodization of a sample prior to breakthrough to the substrate.

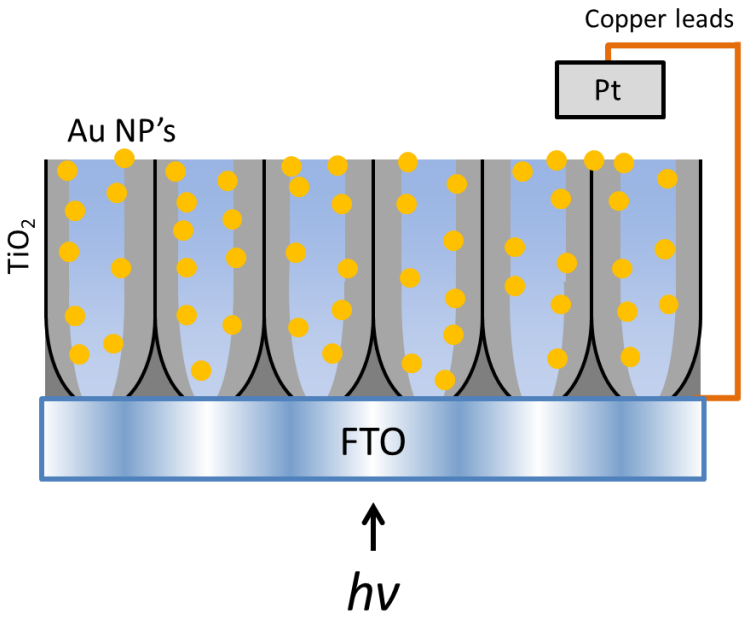

Figure 18: Proposed TNA photoanode on FTO substrate

3.4 Results and Discussion

An unforeseen complication of only performing one anodization is the pore diameter of the TNA remaining about 10nm in diameter. Chemical etching in dilute hydrochloric acid

for various lengths of time allowed for similar pore diameters to those seen in titanium substrate based two-step anodizations, though with less hexagonal ordering. Pore diameters upwards of 70nm can be produced using this etch procedure as shown in Figure 19 C.

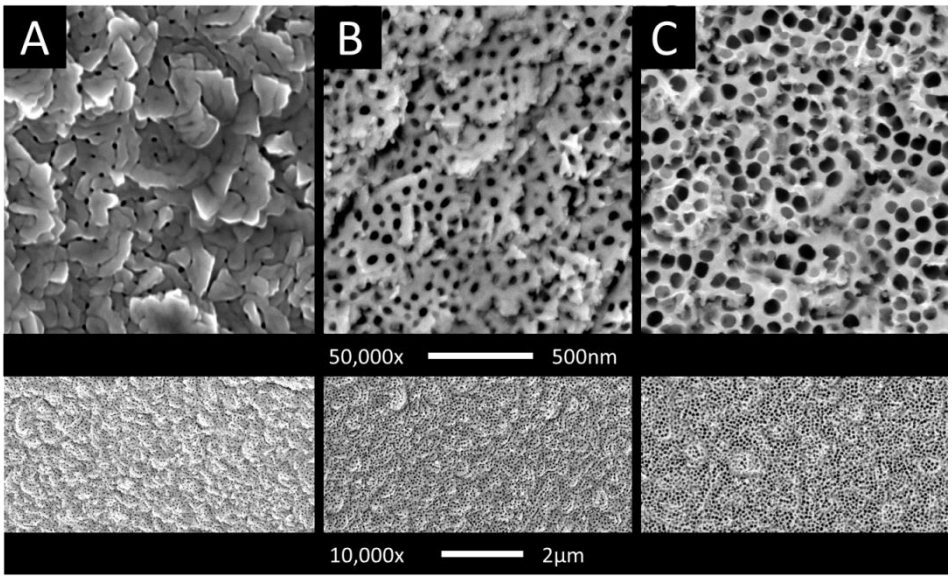

Figure 19: SEM images of TNA on FTO substrate after etching in 2M HCl. A: 0 min B: 30 min. C: 80 min.

The 500nm-1µm thick TNA films with more porous bottoms were penetrated by the gold electrodeposition solution, depositing nanoparticles uniformly within the structure (Figure 20 A,B). Larger diameter gold nanoparticles were deposited on the surface suggesting some preference for charge and nucleation to remain at the TNA surface (Figure 20C), similar to the result in titanium coin devices. The more porous barrier layer allowed for extensive deposition at the electrically conductive FTO substrate (Figure 20D). Numerous variations in the current density, pulse length, delay length, solution temperature, and even deposition solution were optimized for consistency and uniform gold nanoparticle loading throughout the TNA films.

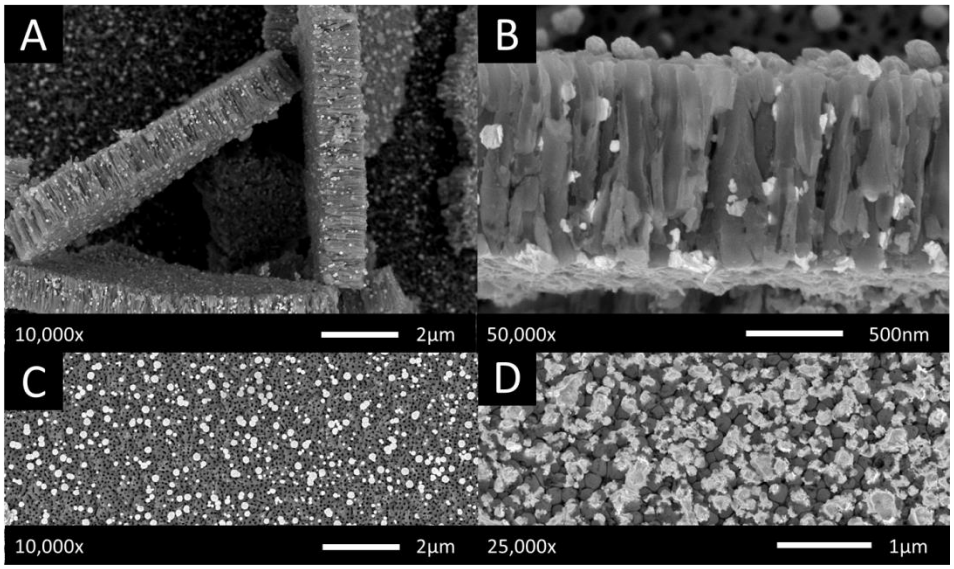

Figure 20: SEM images of TNA on FTO substrate after 30 min etching in 2M HCl. A: Uniform TNA film thickness and AuNP distribution B: TNA cross-section C: Top view D: Bottom view

The FTO-based TNA-AuNP photoanode was tested in a similar manner to the titanium-based photoanode, showing 10-15µA/cm^2 across a similar voltage, supporting the conclusion that gold plasmonically sensitizes titania for the visible portion of the solar

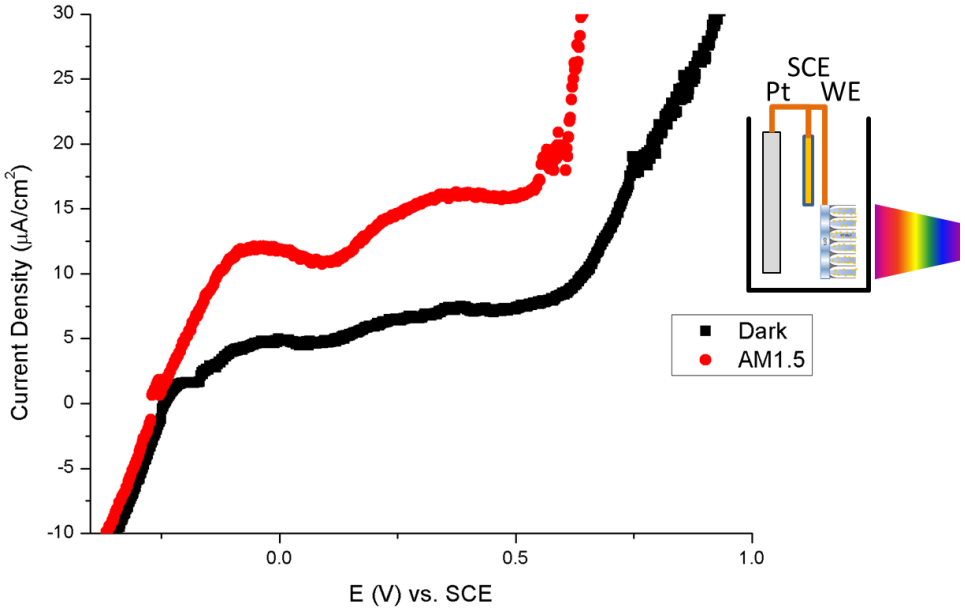

Figure 21: Linear sweep voltammogram of TNA-AuNP photoanode on FTO at 20mV/sec in 1M NaOH normalized for 1 sun AM1.5 solar radiation above 420nm.

spectrum. Transferring the fundamental device design to a quicker and more versatile substrate platform gives credit to the robust nature of this template fabrication method.

Chapter 4: Mesoporous Silica-templated Nanostructured Metal Arrays

4.1 Proposed Structure

Similar in concept to titania nanotube arrays, anodic aluminum oxide (AAO) has been used to generate different plasmonic nanostructures such as nanowires and nanorods. The inspiration for revisiting this method began with a need for unique nanostructure geometries that had a wider plasmon resonance in the visible portion of the solar spectrum. Figure 22 is based on a template within a template fabrication method that combined the confinement effects of the AAO template with a standard block-copolymer silica sol-gel solution.[30]

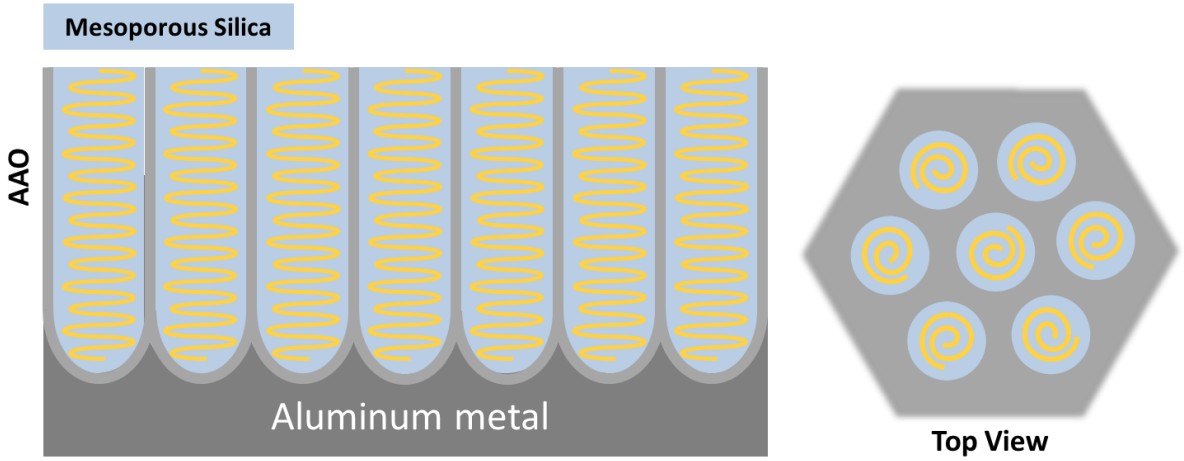

Figure 22: Proposed mesoporous silica-templated plasmonic structures

To date, studies have shown the breadth of these nanostructure formations as a function of AAO pore diameter and their potential application in surface-enhanced Raman spectroscopy. However, there is very little reported on the plasmon resonance of such unique structures, or the possibility of fabricating a photoelectrochemical device from this templating method. The different nanostructures reported using this method were formed via silver electrodeposition, with no reports of gold being attempted. Following a two-step anodization procedure with chemical pore widening, the sol-gel aging, self-assembly, and heat treatment provide a

mesoporous silica template within each AAO pore. This template has approximately a 20nm channel that can be backfilled with an electrodeposited material, and the templates removed with different etching procedures.

4.2 Results and Discussion

The first anodization is etched away using chromic acid, leaving uniform hexagonal dimples in the aluminum surface, preferentially orienting the second anodization in the hexagonal pattern in Figure 22. After a second anodization, the template looks partially blocked in Figure 23A, something remedied with phosphoric acid etching of the template.

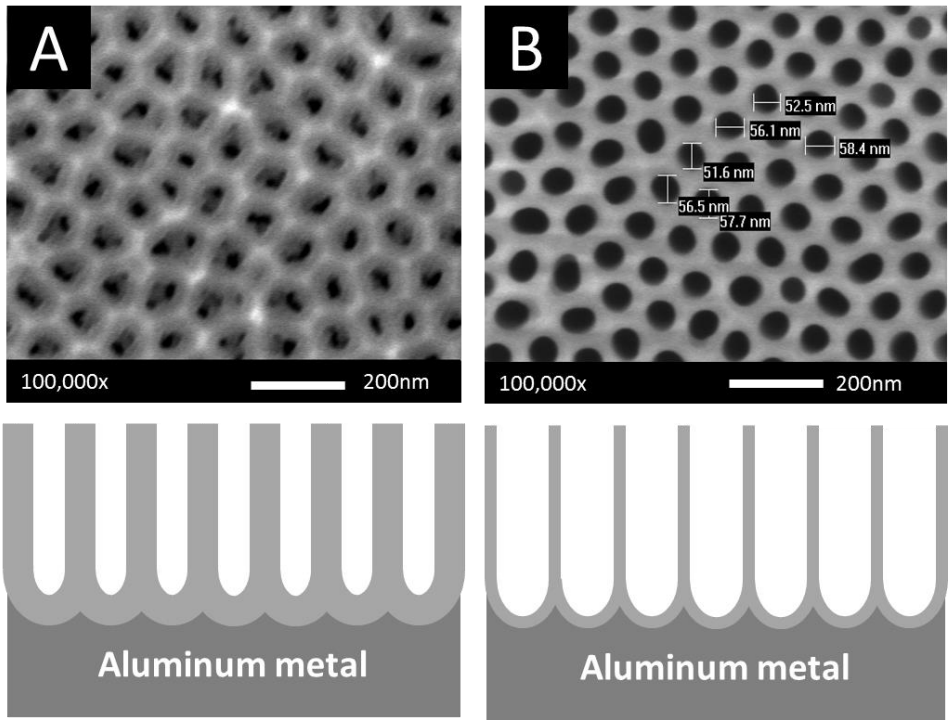

Figure 23: SEM images of A: Second anodization without pore widening at 40V in 0.3M oxalic acid. B: Same sample pore widened by wet chemical etch in 0.2M phosphoric acid for 45 minutes.

The length of time spent etching the film determines the pore diameter between 20nm and 80nm, as well as reduces the barrier layer thickness at the bottom of the AAO pores.

Initial attempts at depositing silver into the mesoporous silica containing AAO template were carried out to verify the original published results. The incomplete formation

of the silica sol-gel in the pores is very evident in all four images in Figure 24, as no distinct helical or stacked doughnut structures are observed. Instead, polycrystalline silver nanowires formed, confirming the AC electrodeposition method for depositing when a barrier layer is present. Slight variation in humidity, temperature, and sol gel components were all proposed as the cause of incomplete structure formation. Exploring the parameter space around the prescribed 1 TEOS:0.0096 P123: 6 H_2O: 8.8 EtOH: 0.001 HCl mole ratios resulted in a successful variation through two modifications. A slightly higher water content of 6.5 relative to TEOS, and a longer sol-gel solution aging time prior to dipcoating produced the desired helical structures as shown in Figure 25. Lastly, the sol-gel generally produced a thick mesoporous silica film on top of the AAO film, making electrodeposition less consistent. A short spin at 3000rpms on a spincoater removed excess solution from the surface without harming structure formation within the pores.

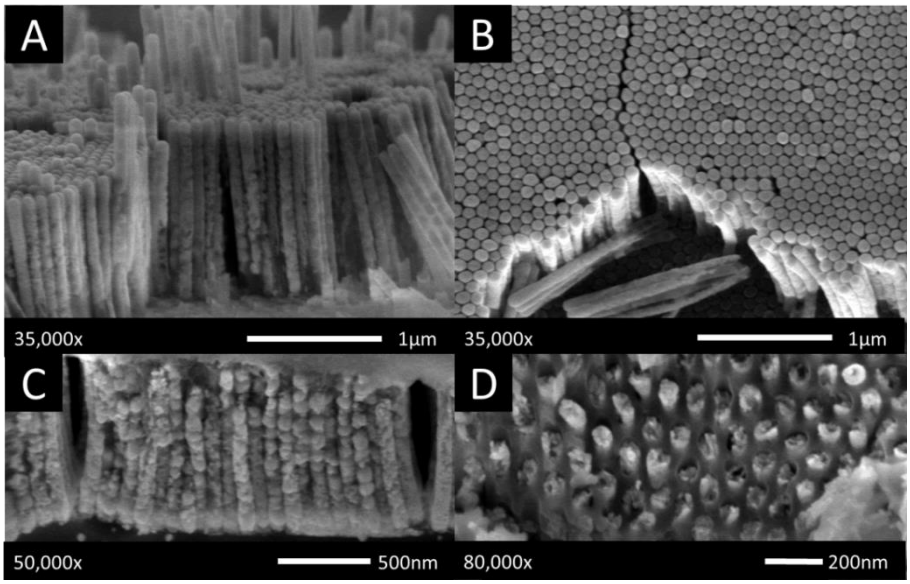

Figure 24: SEM images of incomplete Ag nanowires free of AAO template. A: Cross section B: Bottom view C: Cross section of second sample D: Nearly complete formation within AAO template.

The cross-section enlarged in Figure 25 is enlarged at right with diagonal lines aiding the visualization of the double helical structures clearly embedded in the AAO pores. The pore diameter can vary by as much as 5nm, resulting in a distribution of different

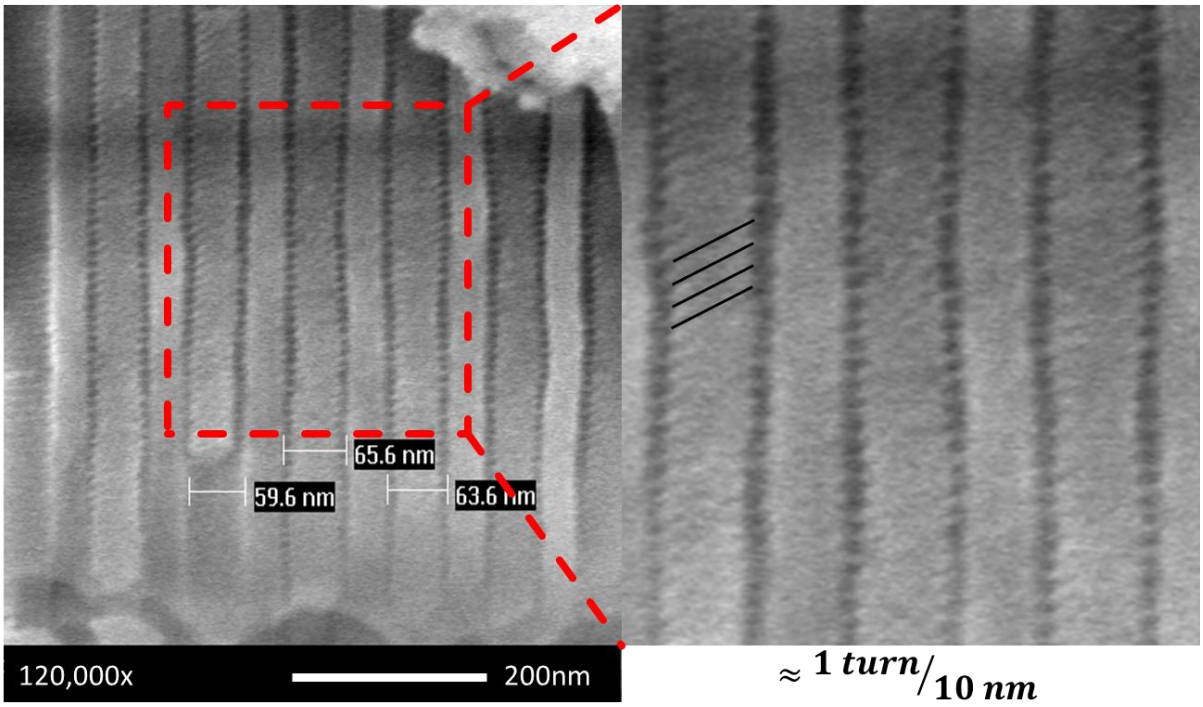

Figure 25: SEM images of double helical mesoporous silica template within AAO template. Enlargement shows angular nature of helical structures.

structures, with most being termed 's-helices' from the original work.[30] The pitch of these chiral structures was confirmed from SEM images to be about 10 nm per turn. This is the first time mesoporous helical silica has been confirmed by scanning electron microscopy without metal electrodeposited as a contrast agent. Helical silver nanostructures were successfully deposited in the silica template as shown in Figure 26 A and B. The top down view in B shows the secondary helical structure inside the outer layer visible in A. Confirmation of these structures by SEM led to optimization of chemical etching steps to remove the anodic alumina template using sodium hydroxide or phosphoric acid. Further processing of each sample was necessary to collect transmission UV-Vis spectra. A section

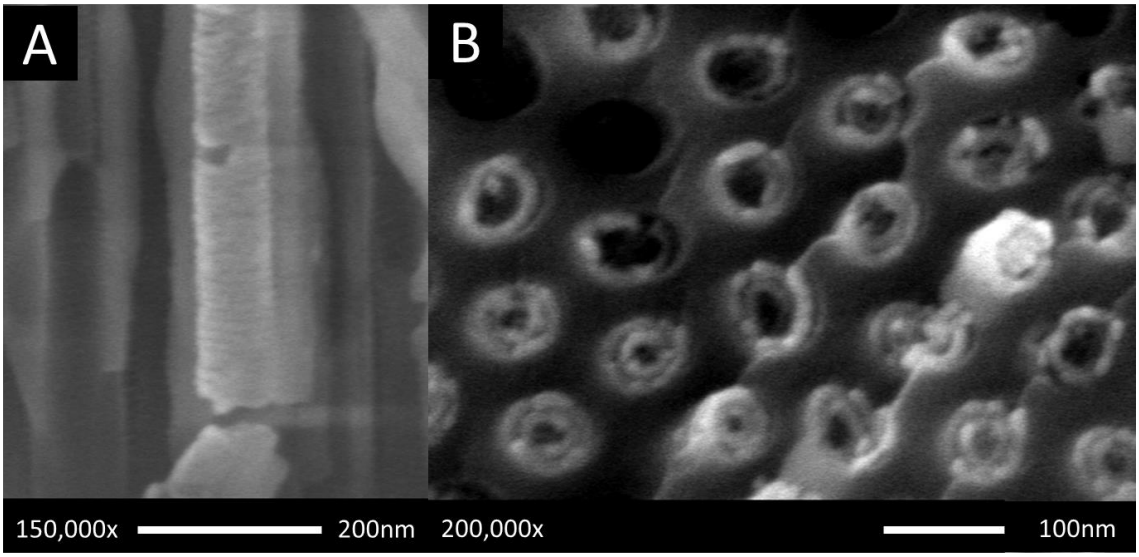

Figure 26: SEM images of A: double doughnut Ag nanowires within AAO template. B: double helical and doughnut Ag nanowires within AAO template

of each sample was encapsulated AAO side down in polydimethylsiloxane polymer and cured, preserving the arrangement of the nanostructures. The absorption of these helical structures extends to 550nm, beyond the plasmon resonance of typical silver nanostructures. This suggests that the unique geometry has an impact on the ability to absorb light of lower energy and generate hot electrons for use in a device.

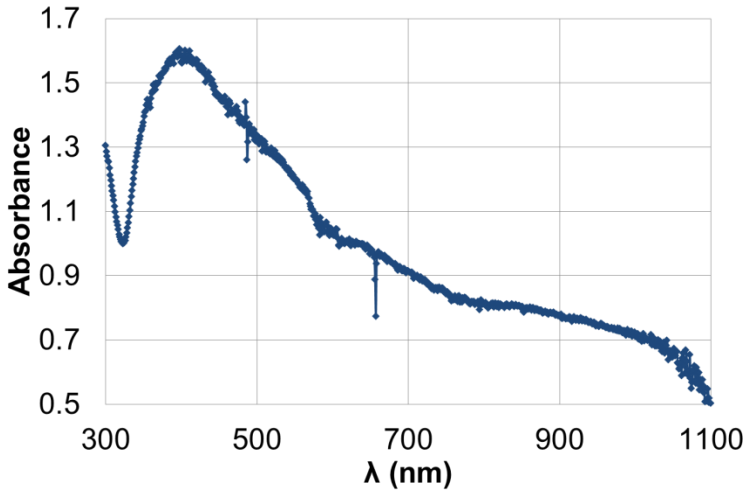

Figure 27: UV-Vis diffuse reflectance spectra showing the surface plasmon resonance of silver extending to 550nm

Chapter 5: Conclusions and Future Work

The proposed plasmonically sensitized gold nanoparticle-titania nanotube arrays were successfully fabricated using titanium metal as a substrate. Determining a consistent synthesis method for the template led to the ammonium fluoride in ethylene glycol electrolyte combination. Electrodeposition proved possible but uncontrollable due to the semiconducting nature of the TNAs. These photoanodes produced measurable photocurrent under simulated visible solar irradiation, however they were not optimized or easily tailored for this application.

A second generation photoanode included top or bottom illumination orientations thanks to the use of a transparent conductive substrate. Replicating the pore diameter through chemical etching improved upon the days required for two-step anodization and reduced them to a few hours for the accelerated one-step anodization. The precise control over the TNA film thickness allowed for more uniform electrodeposition of gold nanoparticles. Photoelectrochemical testing confirmed the visible spectrum absorption of light and the generation of photocurrent. The general concept of using titania nanotube arrays sensitized plasmonically with gold was shown in two different but scalable and efficient fabrication schemes. In particular, the second architecture is a good foundation because it can quickly be adapted to different device arrangements as desired.

Anodic aluminum oxide templates were used as a versatile template for the generation of an in-situ secondary template from a silica sol-gel solution. The mesoporous silica that formed inside the AAO pores was reproduced successfully and confirmed using scanning electron microscopy. The deposition of silver nanostructures and their release from the template was also optimized for characterization purposes. Promising initial results from

UV-Vis spectroscopy show the plasmon resonance of these silver structures extending well into the green portion of the visible spectrum at about 550nm. These results are encouraging for future study of different electrodeposited metals using these templates, as well as varying nanostructure type via smaller AAO pore diameters.

One of the challenges with the AAO template remains the consistent removal of the barrier layer when using an aluminum substrate. Multiple methods have been reported though consistent results for successful DC or pulsed DC electrodeposition remain difficult to reproduce. Ohmic contact to these unique structures in a gold or silver arrangement would allow for the device to be finished with an electron filtering semiconductor such as titania and finished with a hydrogen evolution catalyst such as platinum. The envisioned device is presented in Figure 28. This would function as a photocathode, though various modifications can be made for hot electron harvesting from these nanostructures once the foundation is clearly established.

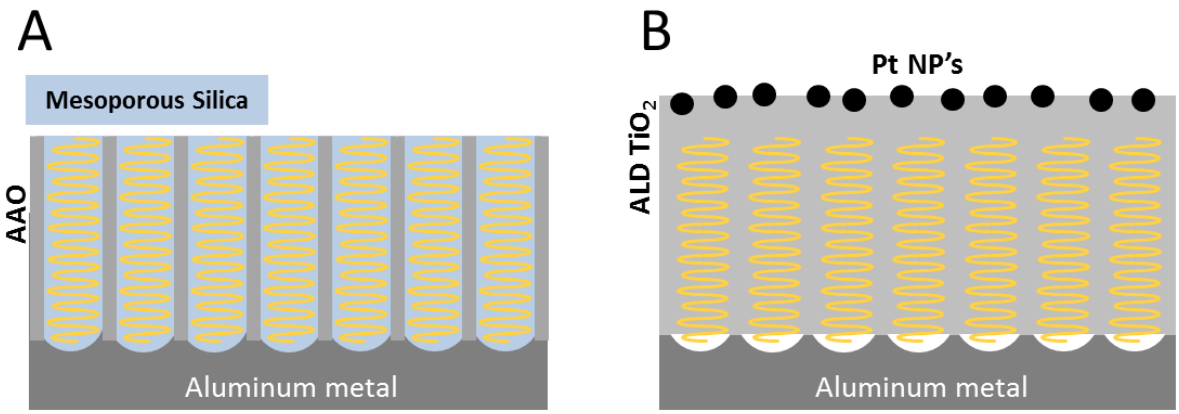

Figure 28: A: Barrier layer removal enables ohmic contact to plasmonic nanostructures for photoelectrochemical testing. B: Finished device with atomic layer deposited titania as an electron filter and platinum nanoparticles as a hydrogen evolution catalyst (B).

This work is a necessary first step in determining what light harvesting structures can be used in a scalable, robust, and cost-effective manner for driving solar to fuel conversion

reactions. Only with fundamental research into materials and their properties can new avenues for the production of hydrogen through water splitting, or the recycling of carbon dioxide into fuel, be realized.

Chapter 6: References

1. Richter, B., *Energy & Environmental Science* **2012,** *5* (9), 8758-8759.
2. Protti, S.; Albini, A.; Serpone, N., *Physical Chemistry Chemical Physics* **2014,** *16* (37), 19790-19827.
3. Liu, C.; Dasgupta, N. P.; Yang, P. D., *Chemistry of Materials* **2014,** *26* (1), 415-422.
4. Wang, H.; Chu, D.; Miller, E. L., *Electrochemical Society Interface* **2013**, 69.
5. Peharz, G.; Dimroth, F.; Wittstadt, U., *International Journal of Hydrogen Energy* **2007,** *32* (15), 3248-3252.
6. Licht, S.; Wang, B.; Mukerji, S.; Soga, T.; Umeno, M.; Tributsch, H., *International Journal of Hydrogen Energy* **2001,** *26* (7), 653-659.
7. Mubeen, S.; Singh, N.; Lee, J.; Stucky, G. D.; Moskovits, M.; McFarland, E. W., *Nano Letters* **2013,** *13* (5), 2110-2115.
8. Photosynthesis, J. C. f. A. Solar Fuels. http://solarfuelshub.org/research/ (accessed May 27th).
9. Chen, S. Y.; Wang, L. W., *Chemistry of Materials* **2012,** *24* (18), 3659-3666.
10. Hu, S.; Shaner, M. R.; Beardslee, J. A.; Lichterman, M.; Brunschwig, B. S.; Lewis, N. S., *Science* **2014,** *344* (6187), 1005-1009.
11. Hayashi, S.; Okamoto, T., *Journal of Physics D-Applied Physics* **2012,** *45* (43).
12. Willets, K. A.; Van Duyne, R. P., *Annual Review of Physical Chemistry* **2007,** *58*, 267-297.
13. Clavero, C., *Nature Photonics* **2014,** *8* (2), 95-103.
14. Linic, S.; Christopher, P.; Ingram, D. B., *Nature Materials* **2011,** *10* (12), 911-921.
15. Mubeen, S.; Lee, J.; Liu, D. Y.; Stucky, G. D.; Moskovits, M., *Nano Letters* **2015,** *15* (3), 2132-2136.
16. Leenheer, A. J.; Narang, P.; Lewis, N. S.; Atwater, H. A., *Journal of Applied Physics* **2014,** *115* (13).
17. Mubeen, S.; Lee, J.; Singh, N.; Kraemer, S.; Stucky, G. D.; Moskovits, M., *Nature Nanotechnology* **2013,** *8* (4), 247-251.
18. Moskovits, M., *Nature Nanotechnology* **2015,** *10* (1).

19. Prevot, M. S.; Sivula, K., *Journal of Physical Chemistry C* **2013,** *117* (35), 17879-17893.
20. Rani, S.; Roy, S. C.; Paulose, M.; Varghese, O. K.; Mor, G. K.; Kim, S.; Yoriya, S.; LaTempa, T. J.; Grimes, C. A., *Physical Chemistry Chemical Physics* **2010,** *12* (12), 2780-2800.
21. Mor, G. K.; Varghese, O. K.; Wilke, R. H. T.; Sharma, S.; Shankar, K.; Latempa, T. J.; Choi, K.-S.; Grimes, C. A., *Nano Letters* **2008,** *8* (7), 1906-1911.
22. Liu, Z.; Hou, W.; Pavaskar, P.; Aykol, M.; Cronin, S. B., *Nano Letters* **2011,** *11* (3), 1111-1116.
23. Lee, K.; Hahn, R.; Schmuki, P., *Electrochemistry Communications* **2014,** *43*, 105-108.
24. Xiao, F., *Journal of Physical Chemistry C* **2012,** *116* (31), 16487-16498.
25. Chen, Y.; Tian, G.; Pan, K.; Tian, C.; Zhou, J.; Zhou, W.; Ren, Z.; Fu, H., *Dalton Transactions* **2012,** *41* (3), 1020-1026.
26. Alkire, R. C.; Gogotsi, Y.; Simon, P.; Eftekhari, A., *Nanostructured materials in electrochemistry*. John Wiley & Sons: 2008.
27. Rabin, O.; Herz, P. R.; Lin, Y. M.; Akinwande, A. I.; Cronin, S. B.; Dresselhaus, M. S., *Advanced Functional Materials* **2003,** *13* (8), 631-638.
28. Musselman, K. P.; Mulholland, G. J.; Robinson, A. P.; Schmidt-Mende, L.; MacManus-Driscoll, J. L., *Advanced Materials* **2008,** *20* (23), 4470-4475.
29. Lee, J.; Mubeen, S.; Ji, X.; Stucky, G. D.; Moskovits, M., *Nano Lett.* **2012,** *12* (9), 5014- 5019.
30. Wu, Y. Y.; Cheng, G. S.; Katsov, K.; Sides, S. W.; Wang, J. F.; Tang, J.; Fredrickson, G. H.; Moskovits, M.; Stucky, G. D., *Nature Materials* **2004,** *3* (11), 816-822.
31. Wu, Y. Y.; Livneh, T.; Zhang, Y. X.; Cheng, G. S.; Wang, J. F.; Tang, J.; Moskovits, M.; Stucky, G. D., *Nano Letters* **2004,** *4* (12), 2337-2342.
32. Liu, N.; Lee, K.; Schmuki, P., *Angewandte Chemie-International Edition* **2013,** *52* (47), 12381-12384.
33. Nielsch, K.; Muller, F.; Li, A. P.; Gosele, U., *Advanced Materials* **2000,** *12* (8), 582-586.

34. Sauer, G.; Brehm, G.; Schneider, S.; Nielsch, K.; Wehrspohn, R. B.; Choi, J.; Hofmeister, H.; Gosele, U., *Journal of Applied Physics* **2002,** *91* (5), 3243-3247.